# On the dynamics of the large scale circulation in turbulent convection with a free-slip upper boundary

Joauma Marichal and Miltiadis V. Papalexandris

*Université catholique de Louvain*
*Institute of Mechanics, Materials and Civil Engineering*
*1348 Louvain-la-Neuve, Belgium*

**Abstract**

In this paper we present a numerical study of the dynamics of the Large-Scale Circulation (LSC) in turbulent convection with a free surface. Our study is based on Large-Eddy Simulations of thermal convection in a cube with a heated bottom wall and a cooled free-slip upper boundary which approximates the free surface. With water as the working fluid, simulations are performed at two different Rayleigh numbers, $Ra = 2\times10^7$ and $Ra = 1\times10^8$. The LSC is the principal convective structure and is driven by plume formation at the top and bottom boundaries. In cuboidal domains, the LSC orientates itself along one of the diagonal planes. However, neither the orientation plane nor the direction of circulation remain fixed with time and reorientation events occur. Herein we first present the basic features of the LSC and then examine the frequency of reorientations and their role in turbulence statistics. According to our simulations, the most frequent event is the change of orientation plane, whereas changes in the direction of circulation are scarce. Also, the frequency of reorientations reduces significantly as the Rayleigh number increases. Finally, our analysis shows that reorientation events have an impact on the root-mean-square of the fluctuating components of the horizontal velocity. Therefore, statistics should be taken over long time periods so as to account for a sufficiently large number of events.

*Keywords:* Rayleigh-Bénard convection, thermal convection, free surface, reorientations, Large Eddy Simulations, non-Oberbeck–Boussinesq conditions.

*Preprint submitted to International Journal of Heat and Mass Transfer October 26, 2021*

## 1. Introduction

In this paper, we present results from Large-Eddy Simulations (LES) of turbulent thermal convection in a cuboidal domain with a free-surface upper boundary. Thermal convection of this type occurs naturally, for example in oceans and lakes, and in a wealth of industrial and technological applications. The flow in question has similarities to turbulent Rayleigh–Bénard convection (RBC). In this latter flow, a Large Scale Circulation (LSC) emerges, driven by plume formation at the top and bottom boundaries.

The configuration of the LSC depends on the shape of the container [1, 2] and has been the subject of experimental and numerical research for many years [3]. Such studies have improved our understanding of the structure of the LSC [2, 4, 5, 6, 7] and its dynamic behavior for various working fluids within 2D rectangular [8, 9], 2D circular [10], 3D cubical [2, 4, 11] and 3D cylindrical geometries [12, 13, 14]. The LSC has been shown to change its orientation in an apparently random manner [15, 16, 17, 18] and many questions remain unanswered with regard to its dynamics. This paper brings insight on the frequency of reorientations and their relation with the free-slip boundary condition. It also investigates the influence of these events on turbulence statistics.

One of the earliest accounts of LSC reorientations was reported by Cioni et al. [12] who studied convection of mercury in a cylindrical container at $Pr = 0.025$. Since then, experimental studies have focused predominately on cylindrical geometries where two types of reorientation events have been distinguished [14]. The first is *rotations*, which involve the rotation of the LSC orientation plane and the second is *cessations*, which are characterized by an interruption of the LSC and its reappearance in another orientation shortly after. Experimental and numerical studies in 2D rectangular geometries reported in [8] have highlighted the role of smaller convection structures on reorientations.

However, the complexity of the problem is greatly increased in cubic geometries. The latter configuration has been addressed in [2] and [11] for air at $Pr = 0.7$. The authors of [2] have analyzed the complete flow topology via Large-Eddy Simulations (LES) in a cube and defined the corresponding reorientation frequency using probes. Also, the authors of [11] reported that reorientation events are more likely at lower Rayleigh numbers, $Ra$. Indeed, the corner roll tend to shrink as $Ra$ increases, leading to a more stable LSC.

Our study performs a similar analysis of reorientations in a cube. The working fluid is water, which is heated from below and cooled at the free surface above, approximated herein as a free-slip boundary. This configuration is referred to herein as FS. Simulations of classical turbulent RBC in a cubic domain, herein referred to simply as RBC, are also performed for comparative purposes. Rayleigh numbers of $Ra = 2 \times 10^7$ and $Ra = 1 \times 10^8$ are investigated and statistics are taken over 15 000 $t_{\mathrm{ff}}$, with $t_{\mathrm{ff}}$ being the free-fall time. This averaging time is at least an order of magnitude longer than most other numerical simulations in the field and allows for novel insight into the long-term effects of reorientations on the flow statistics.

The paper is structured as follows. In Section 2 we present the mathematical model for the flows of interest and outline the algorithm for its numerical treatment. Then, in Section 3 we describe the numerical set-up of our simulations. Section 4 contains the presentation and analysis of numerical results, where we first explain the global properties of the flow before elaborating on the reorientation events and their characteristics. Subsequently, we present the turbulence statistics and investigate the impact of reorientations on them. Finally, conclusions are drawn in Section 5.

## 2. Governing Equations

With regard to the fluid density, the Oberbeck–Boussinesq approximation is invoked in most studies on natural convection. However, for the cases considered herein, the variations of the thermo-physical properties of the working fluid (water) with the temperature are no longer negligible. Accordingly, the system of governing equations is the low-Mach number approximation of the compressible Navier-Stokes-Fourier equations [19, 20]. This system is then Favre filtered, as is typical in variable-density LES. Applied to a generic quantity $\phi$, the corresponding Favre-filtered quantity $\widetilde{\phi}$ is given as $\widetilde{\phi} = \frac{\overline{\rho\phi}}{\overline{\rho}}$, where $\overline{\rho}$ and $\overline{\rho\phi}$ are spatially filtered quantities. Following this procedure, the filtered governing equations read, in dimensional form,

$$\frac{\partial \overline{\rho}}{\partial t} + \boldsymbol{\nabla}\cdot\left(\overline{\rho}\widetilde{\boldsymbol{u}}\right) = 0\,, \tag{1}$$

$$\frac{\partial\left(\overline{\rho}\widetilde{\boldsymbol{u}}\right)}{\partial t} + \boldsymbol{\nabla}\cdot\left(\overline{\rho}\widetilde{\boldsymbol{u}}\widetilde{\boldsymbol{u}}\right) = -\boldsymbol{\nabla}\overline{p} + \boldsymbol{\nabla}\cdot\left(2\mu\widetilde{\boldsymbol{S}}\right) - \boldsymbol{\nabla}\cdot\boldsymbol{\tau}^{\mathrm{r}} + \overline{\rho}\boldsymbol{g}\,, \tag{2}$$

$$\frac{\partial \overline{\rho} c_p \widetilde{T}}{\partial t} + \boldsymbol{\nabla}\cdot\left(\overline{\rho} c_p \widetilde{\boldsymbol{u}}\widetilde{T}\right) = \frac{\mathrm{d}p_0\left(t\right)}{\mathrm{d}t} + \boldsymbol{\nabla}\cdot\left(\kappa\boldsymbol{\nabla}\widetilde{T}\right) + \boldsymbol{\nabla}\cdot\boldsymbol{q}^{\mathrm{r}}\,, \tag{3}$$

where $\overline{\rho}$, $\widetilde{\boldsymbol{u}} = (\widetilde{u}, \widetilde{v}, \widetilde{w})$ and $\widetilde{T}$ stand for the filtered fluid density and the Favre-filtered velocity vector and temperature, respectively. Further, in equation (2), $\overline{p}$ is the sum of the dynamic and bulk-viscous pressures [21, 22], the dynamic pressure being the second term of the asymptotic expansion of the fluid pressure at low Mach numbers. On the other hand, $p_0(t)$ stands for the first term of the asymptotic expansion and is interpreted as the thermodynamic pressure. According to low-Mach-number asymptotics, $p_0(t)$ is spatially uniform and a function of time only. For the flows under study, $p_0$ is constant and equal to the ambient pressure. Also, $\boldsymbol{g}$ denotes the gravitational acceleration.

Further, the second term of the right-hand side of equation (2) describes the filtered viscous stresses. Therein, $\mu$ is the dynamic viscosity and $\widetilde{\boldsymbol{S}}$ is the deviatoric component of the filtered strain-rate tensor, $\widetilde{\boldsymbol{S}} = \frac{1}{2}\left(\boldsymbol{\nabla}\widetilde{\boldsymbol{u}} + (\boldsymbol{\nabla}\widetilde{\boldsymbol{u}})^{\top}\right) - \frac{1}{3}(\boldsymbol{\nabla}\cdot\widetilde{\boldsymbol{u}})\mathbf{I}$ with $\mathbf{I}$ being the identity matrix. Finally, in equation (3), the second term of the right-hand side is the filtered heat flux. The specific heat capacity is denoted by $c_p$ and $\kappa$ stands for the thermal conductivity.

The above system is closed with an isobaric "equation of state", $\overline{\rho}(\widetilde{T})$. In our study, we employ a seventh-order polynomial fit of tabulated data from [23] for water density at the ambient pressure and over the temperature range of interest. The two transport coefficients, $\kappa$ and $\mu$ are also calculated from a seventh-order polynomial fit with data originating from [23]. The variation of the specific heat capacity $c_p$ across the flow domain is less than 2%. Nonetheless, for our simulations, we also opted for a polynomial fit, on the basis of data from [23].

According to the LES approach, the large scales of the flow are resolved by the computational grid, whereas the effects of the smaller ones are suitably modeled. For this reason, LES grids are much coarser than their counter-

parts in Direct Numerical Simulations (DNS), which offers significant computational savings. These savings are essential for the purposes of this study because they enable to run the simulations over sufficiently long times so as to register a large number of LSC reorientations. In equations (2) and (3), the unresolved terms that emerge after filtering are the subgrid scale stress tensor $\boldsymbol{\tau}^{\mathrm{r}}$ and subgrid scale heat flux $\boldsymbol{q}^{\mathrm{r}}$, defined as,

$$\boldsymbol{\tau}^{\mathrm{r}} \;=\; \overline{\rho}(\widetilde{\boldsymbol{u}}\widetilde{\boldsymbol{u}} - \widetilde{\boldsymbol{u}\boldsymbol{u}})\,, \tag{4}$$

and

$$\boldsymbol{q}^{\mathrm{r}} \;=\; \overline{\rho}\left(\widetilde{\boldsymbol{u}}\widetilde{T} - \widetilde{\boldsymbol{u}T}\right)\,, \tag{5}$$

respectively. A very common approach for the representation of these terms is the eddy-viscosity model which is elaborated in standard textbooks; see, for example, [24, 25, 26]. According to this approach, these terms are modeled, respectively, as additional viscous stresses and diffusive transport, that is,

$$\boldsymbol{\tau}^{\mathrm{r}} - \frac{1}{3}\mathrm{Tr}(\boldsymbol{\tau}^{\mathrm{r}}) \;=\; -2\mu_{\mathrm{t}}\widetilde{\boldsymbol{S}}\,, \tag{6}$$

and

$$\boldsymbol{q}^{\mathrm{r}} \;=\; \lambda_{\mathrm{t}}\boldsymbol{\nabla}\widetilde{T}\,. \tag{7}$$

The residual kinetic energy term in equation (6), $\frac{1}{3}\mathrm{Tr}(\boldsymbol{\tau}^{\mathrm{r}})$, is incorporated in the pressure term $\overline{p}$ of equation (2).

For the computation of the eddy viscosity $\mu_{\mathrm{t}}$, we employ the dynamic one-equation eddy-viscosity model, according to which

$$\mu_{\mathrm{t}} \;=\; C_s\, k^{1/2}\,\Delta\,. \tag{8}$$

In this equation, $C_s$ is the model constant and is computed via the dynamic procedure described in [27, 28]. The subgrid kinetic energy $k$ is obtained by solving numerically its transport equation. Also, $\Delta$ stands for the cell size. In our study, it is set equal to the computational cell size which is defined as the cubic root of the volume of the computational cell, $\Delta = (\Delta x\,\Delta y\,\Delta z)^{1/3}$.

Finally, the eddy conductivity is computed via the Reynolds analogy, according to which

$$\lambda_{\mathrm{t}} \;=\; \mu_{\mathrm{t}} c_p / Pr_{\mathrm{t}}\,, \tag{9}$$

where $Pr_{\mathrm{t}}$ is the turbulent Prandtl number. In our study, $Pr_{\mathrm{t}}$ is taken constant and equal to 0.4; this is the same value as the one used in [29].

The low-Mach-number equations (1)–(3) are discretized and solved numerically via a second-order time-integration scheme that uses the values of the convective and diffusive terms in the current and the two previous time-steps. With regard to spatial discretization, both the convective and diffusive terms are discretized via second-order central differences. The equations are solved on a collocated grid system. In order to avoid the well-known pressure odd-even decoupling associated with such grids, we employ the flux-interpolation technique described in [20, 30], which is a generalization of the original Rhie-Chow scheme [31] to variable-density flows.

For the computation of the pressure-velocity coupling we employ a PISO-type projection method, which is also a generalization of the original Pressure-Implicit with Splitting of Operators (PISO) algorithm [32, 33] for constant-density flows. According to it, the divergence of the momentum equation and the continuity equation are combined to derive a linear elliptic partial differential equation for $\overline{p}$ that includes the temporal derivative of the density $\frac{\partial \overline{\rho}}{\partial t}$ on its left-hand side. For more details, the reader is referred to [7, 34].

## 3. Numerical Setup

We consider turbulent convection of water in a cubic pool of height $h$. The water is heated from the bottom wall which is located at $y = 0$ and maintained at temperature $T_\mathrm{h}$. The side walls of the pool are adiabatically isolated. No-slip kinematic condition is prescribed at the bottom and side walls, while the free surface of the water is approximated as a free-slip plane. Accordingly, the upper-boundary condition for the velocity reads, $\frac{\partial u}{\partial y} = \frac{\partial w}{\partial y} = 0$ at $y = h$. Further, the free surface is maintained at temperature $T_\mathrm{c}$ which is lower than $T_\mathrm{h}$. For comparison purposes, we also examine the corresponding RBC cases in which the free-slip upper boundary is replaced by a no-slip rigid wall.

The reference temperature $T_\mathrm{ref}$ is defined as the mean between the top and bottom temperatures, $T_\mathrm{ref} = (T_\mathrm{h}+T_\mathrm{c})/2$, while the reference temperature difference is defined as $\Delta T = T_\mathrm{h} - T_\mathrm{c}$. In our study we set $T_\mathrm{ref} = 353.15$ K and $\Delta T = 10$ K. The thermo-physical properties of water at $T_\mathrm{ref}$ are provided in Table 1.

Turbulent convection is parameterized with respect to three dimensionless groups. These are the Rayleigh and Prandtl numbers, defined as

$$Ra \;=\; \frac{g\,\beta_\mathrm{ref}\,h^3\,\Delta T}{\nu_\mathrm{ref}\,\kappa_\mathrm{ref}}\,, \quad \text{and} \quad Pr \;=\; \frac{\nu_\mathrm{ref}}{\alpha_\mathrm{ref}}\,, \tag{10}$$

| $T_{\text{ref}}$ $[K]$ | $\Delta T$ $[K]$ | $\rho_{\text{ref}}$ $\left[\frac{kg}{m^3}\right]$ | $\beta_{\text{ref}}$ $\left[\frac{1}{K}\right]$ | $\mu_{\text{ref}}$ $\left[\frac{m^2}{s}\right]$ | $\kappa_{\text{ref}}$ $\left[\frac{m^2}{s}\right]$ | $c_p$ $\left[\frac{J}{kgK}\right]$ |
|---|---|---|---|---|---|---|
| 353.15 | 10 | $9.72 \times 10^2$ | $6.36 \times 10^{-4}$ | $3.54 \times 10^{-4}$ | $6.67 \times 10^{-1}$ | $4.2 \times 10^3$ |

Table 1: Reference temperature $T_{\text{ref}}$, temperature difference $\Delta T$, density $\rho_{\text{ref}}$, thermal expansion coefficient $\beta_{\text{ref}}$, dynamic viscosity $\mu_{\text{ref}}$, thermal conductivity $\kappa_{\text{ref}}$ and heat capacity $c_p$ of water. The corresponding Prandtl number is $Pr = 2.23$.

respectively, and the aspect (width-to-height) ratio of the pool. At the reference temperature, $T_{\text{ref}} = 353.15$ K, the Prandtl number is found to be $Pr = 2.23$, while the aspect ratio is fixed to unity. Also, as mentioned in section 1, we perform simulations at two different Rayleigh numbers, $Ra = 2 \times 10^7$ and $Ra = 1 \times 10^8$, that correspond to different values of the height of the pool, $h$.

For purposes of non-dimensionalization, the height $h$, free-fall velocity $u_{\text{ff}} = \sqrt{\beta_{\text{ref}}\, g\, h\, \Delta T}$ and free-fall time $t_{\text{ff}} = h/u_{\text{ff}}$ are used as the reference length, velocity and time unit, respectively. Their values for the two Rayleigh numbers considered herein are provided in Table 2.

| $Ra$ | $h$ $[cm]$ | $u_{\text{ff}}$ $\left[\frac{cm}{s}\right]$ | $t_{\text{ff}}$ $[s]$ |
|---|---|---|---|
| $2 \times 10^7$ | 2.67 | 4.08 | 0.655 |
| $1 \times 10^8$ | 4.57 | 5.34 | 0.856 |

Table 2: Domain height $h$, free-fall velocity $u_{\text{ff}}$, and free-fall time $u_{\text{ff}}$ for the two Rayleigh numbers considered herein.

With regard to grid-resolution requirements, in the boundary-layer regions we employ the criterion of Shiskina *et al.* [35] for wall-resolved numerical simulations which is based on the laminar Prandtl–Blasius boundary layer theory. According to this criterion, the minimum number of cells for the discretization of the hydrodynamic and thermal boundary layers, $N_u$ and $N_\theta$, are given in terms of the Nusselt and Prandtl number of the flow,

$$N_u \;=\; \sqrt{2}\; a\; Nu^{1/2}\; Pr^{\xi}\,, \tag{11}$$

and

$$N_\theta \;=\; \sqrt{2}\; a\; Nu^{1/2}\; Pr^{\psi}\,, \tag{12}$$

where $Nu$ stands for the global Nusselt number, $\xi = 0.3215 + 0.011 \ln(Pr)$, $\psi = -0.0355 + 0.033 \ln(Pr)$ and $a = 0.482$. The minimum values of $N_u$

and $N_\theta$ resulting from the above relations and the values actually used in our simulations are provided in Table 3. It can be verified that the criterion of [35] is satisfied in all cases considered herein and for both thermal and hydrodynamic boundary layers.

| $Ra$ | Type | $N$ | $N_u$ | $N_\theta$ | $\frac{\Delta_{min}}{h}$ $\times 10^{-2}$ | $\frac{\Delta_{max}}{h}$ $\times 10^{-2}$ | $\frac{\eta_l}{2h}$ $\times 10^{-2}$ | $\frac{4\pi\eta_\theta}{h}$ $\times 10^{-2}$ |
|---|---|---|---|---|---|---|---|---|
| $2 \times 10^7$ | RBC | $50^3$ | 9 (4) | 8 (3) | 0.10 | 5.52 | 6.11 | 7.08 |
| | FS | $46^3$ | 5 (5) | 5 (4) | 0.22 | 5.08 | 5.34 | 6.64 |
| $1 \times 10^8$ | RBC | $74^3$ | 11 (5) | 10 (4) | 0.06 | 3.80 | 4.44 | 4.18 |
| | FS | $70^3$ | 7 (6) | 5 (5) | 0.12 | 3.48 | 3.84 | 3.90 |

Table 3: Grid-resolution criteria. $N$ is the number of cells. $N_u$ and $N_\theta$ stand for the number of cells inside the hydrodynamic and thermal boundary layers, respectively; the values without parenthesis are the actual numbers of cells in the computational grid, while the values in parenthesis are the minimum requirements according to (11) and (12). $\frac{\Delta_{min}}{h}$ and $\frac{\Delta_{max}}{h}$ are the smallest and largest cell size. Finally, $\frac{\eta_l}{2h}$ and $\frac{4\pi\eta_\theta}{h}$ are half the Taylor microscale and the relaxed temperature microscale, respectively.

For determining the resolution requirements in the bulk of the computational domain, we employ the same methodology as in [36]. According to it, the largest cell size in the bulk, which is located in the center of the computational domain, is set to be the minimum between half the Taylor microscale and a relaxed temperature microscale (taken as 4 times the size of the corresponding cell in a direct numerical simulation). The Taylor microscale can be approximated by,

$$\frac{\eta_l}{h} \;=\; \frac{\sqrt{15}u^*}{\left(Ra(Nu-1)\right)^{0.5}}\,, \tag{13}$$

with

$$u^* \;=\; \sqrt{0.068Ra^{0.91} + 0.012Ra^{0.96}}\,, \tag{14}$$

whereas the relaxed temperature microscale is given by,

$$\frac{4\pi\eta_\theta}{h} \;=\; \frac{\pi}{\left(RaPrNu\right)^{0.25}}\,. \tag{15}$$

For the computation of the Nusselt number that appears in the above equations, we first perform a preliminary simulation for each case on a grid based on the above criteria and with a first estimate of $Nu$ provided by the following correlation for RBC [17],

$$Nu \;=\; 0.124Ra^{0.309}\,, \qquad \text{(RBC)}\,. \tag{16}$$

Once the grid-resolution requirement for the preliminary simulation is determined, the computational mesh is stretched along the horizontal and vertical directions using a hyperbolic-tangent expansion from the minimum cell size at the boundaries to the maximum in the center of the domain. The preliminary simulation is initialized by assuming the fluid to be at rest and by assigning a linear temperature profile along the vertical direction. The simulation is then run for 300 $t_{\mathrm{ff}}$, where it is assumed that by that time the flow has become statistically stationary. According to [37], this time period is sufficient to wash out all transient effects.

On the basis of the results of the preliminary simulation for each case, we compute the next estimate of $Nu$ upon which we determine the grid-resolution requirements for the main simulation. Next, we stretch the computational mesh in the exact same way as in the preliminary simulation. The grid dimensions, minimum and maximum grid size, as well as the Taylor and relaxed temperature microscales, are provided in Table 3. The initial condition of a main simulation is the instantaneous flow field at the end of the corresponding preliminary simulation (suitably mapped to the grid of the main simulation). Subsequently, averages are taken over a long time period, 15 000 free-fall times ($t_{\mathrm{ff}}$), which permits to access the impact of LSC reorientations to the turbulence statistics.

## 4. Numerical Results and Discussion

In the first part of this section, we briefly analyze the effect of the free-slip upper boundary to the global flow properties and the LSC. In the second part we discuss the characteristics of reorientation events of the LSC. Then, in the third part we elaborate on the impact of these events on turbulence statistics. As mentioned above, results for both RBC and FS are provided and compared against one another.

All quantities are non-dimensionalized with respect to the aforementioned reference values. Further, instead of $T$, we present results for the normalized temperature, $\theta = \frac{T-T_{\mathrm{ref}}}{\Delta T}$. The time average of a generic quantity $\phi$ is denoted by $\langle\phi\rangle$, while the time and area average (*i.e.* across the horizontal plane) is denoted by $\langle\phi\rangle_{xz}$.

### *4.1. Global flow properties*

We first present results for the global (time- and volume-averaged) Nusselt number $Nu$. For RBC, our simulations predicted $Nu = 22.3$ at $Ra = 2\times10^7$,

and $Nu = 36.6$ at $Ra = 1 \times 10^8$. These values are in very good agreement with the correlation (16) of Niemela et al. [17] that is given above. They are also very close to the values predicted in the numerical studies of Foroozani et al. [4] for air at $Pr = 0.7$ and Kaczorowski and Xia [38] for water at $Pr = 4.38$.

For FS, our simulations predicted higher $Nu$ values in FS than for RBC: $Nu = 29$ at $Ra = 2 \times 10^7$, and $Nu = 48$ at $Ra = 1 \times 10^8$. This increase of $Nu$ is attributed to the absence of hydrodynamic boundary layer on the upper boundary which promotes convection [7, 36]. Also, our predictions are in good agreement with the following $Nu - Ra$ correlation for FS proposed in [34], $Nu = 0.178 Ra^{0.301}$. It is worth mentioning that this correlation for FS was derived from simulations with an evaporating free surface, as opposed to a fixed-temperature one that is prescribed in the present study.

The results presented in the remainder of this subsection are time-averaged over a period of 200 $t_{\text{ff}}$ during which no reorientation events took place. This time period is deemed sufficient for extracting the global flow properties of a stable LSC, *i.e.* by excluding the influence of reorientations.

Plots of the time-averaged streamlines for both cases, RBC and FS, and $Ra = 2 \times 10^7$ are presented in Figure 1. From these plots we can infer that the LSC is aligned with one of the diagonal planes of the domain, as is known to be the case for cuboidal domains. In the LSC, high-temperature fluid from the bottom moves upward, whereas lower-temperature fluid coming from the top plunges downward. In Figure 1, we can clearly identify the point at which the LSC impinges on the free surface. Overall, the flow structure in FS is similar to that in RBC. Nonetheless, in FS the temperature in the bulk is lower. Also, contrary to RBC, in FS the size of the secondary recirculation zones, also called corner rolls, at the LSC diagonal plane are not equal. More specifically, the upper secondary recirculation zone is larger than the lower one. This is indicative of the flow asymmetry induced by the free-slip condition.

In Figure 2, we present contour plots of the mean amplitude of the in-plane velocity component $\langle \bar{v} \rangle$ at the two diagonal planes, superposed with the in-plane velocity vectors. These plots highlight the flow asymmetry introduced by the free surface. In particular, contrary to RBC, in FS the counter-rotating vortices at the second diagonal plane do not have the same size. Instead, the upper vortices are larger, which is due to the absence of an upper hydrodynamical boundary layer. From the plots of this figure, we can also reaffirm the asymmetry of the secondary circulation zones at the LSC

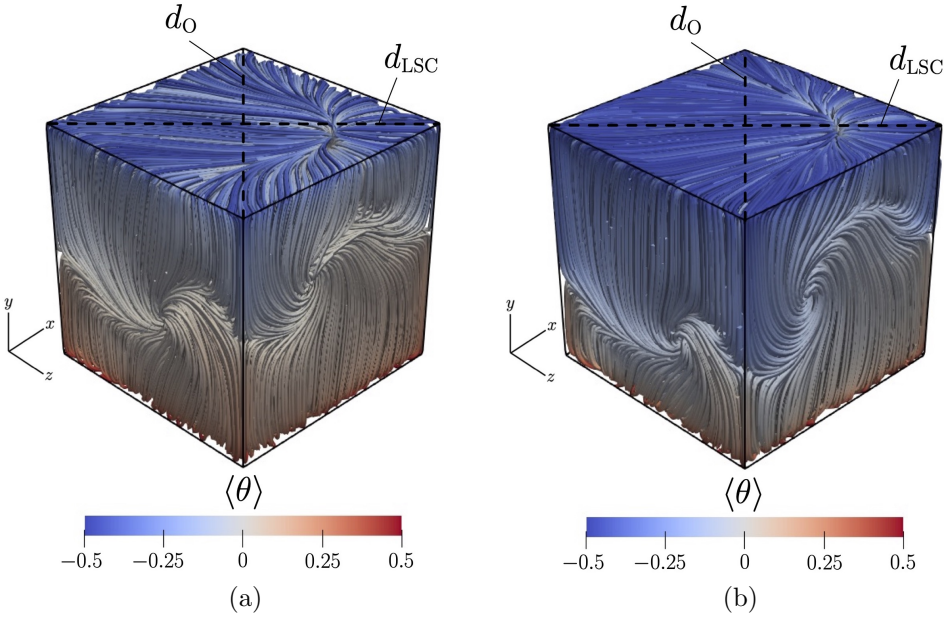
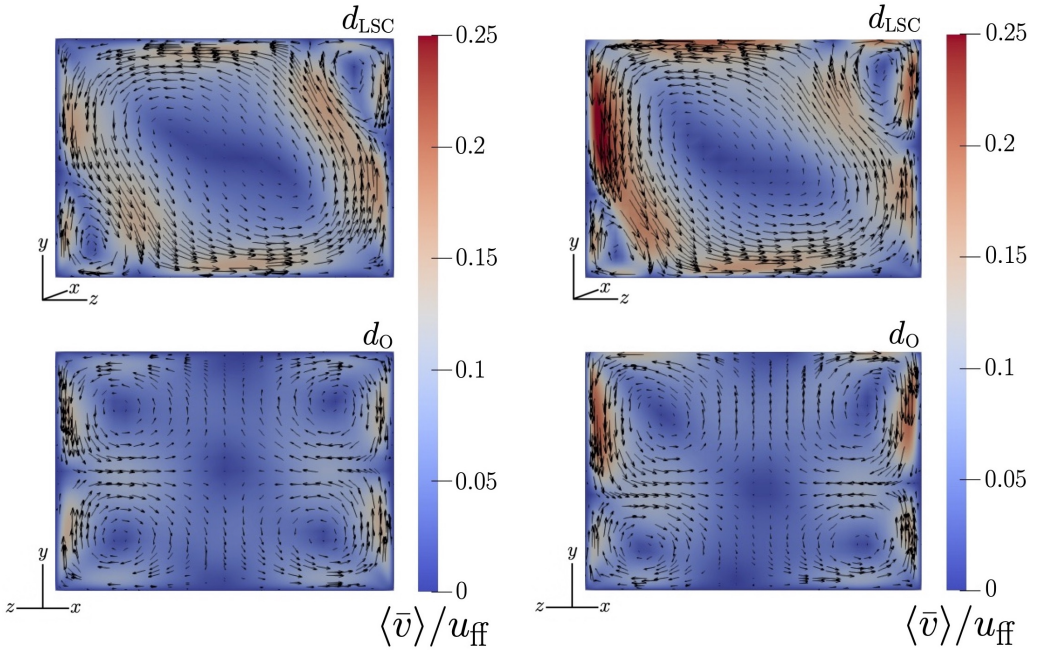



Figure 1: Time-averaged streamlines colored with $\langle\theta\rangle$ at $Ra = 2 \times 10^7$. The LSC plane is denoted by $d_{\mathrm{LSC}}$ and the orthogonal plane by $d_{\mathrm{O}}$. (a) RBC. (b) FS. Overall, the flow structure is similar for both cases; however in FS, the temperature in the bulk is lower. Also, in RBC the size of the secondary recirculation zones at the LSC diagonal plane are equal. In FS, however, this is no longer the case, which is indicative of the flow asymmetry induced by the free-slip upper boundary.

plane, as was mentioned above. Finally, we can observe that the downward motions of the fluid, in the LSC and the secondary vortices of the orthogonal plane, are stronger in FS than in RBC.

Figure 3 contains contour plots of the mean amplitude of the horizontal velocity component, $\langle\bar{u}\rangle = \sqrt{\langle u\rangle^2 + \langle w\rangle^2}$, superposed with the corresponding vector plots, at three different horizontal planes: $y/h = 0.95$, 0.50 and 0.05, respectively. One can observe that in RBC the plots at the planes $y/h = 0.95$ and $y/h = 0.05$ are mirror images of one another. However, this is no longer the case in FS. Moreover, it is clear that the amplitudes of the horizontal velocity component are higher in FS than in RBC. Once again, this is attributed to the free surface which reinforces convective motions by virtue of the absence of an upper hydrodynamic boundary layer. Interestingly though, the velocity amplitude in FS are distinctively higher than in RBC even at the lower horizontal plane $y/h = 0.05$. In other words, the effect of the free surface to the emerging flow patterns is not limited to its vicinity




(a) (b)

Figure 2: Contour plots of the mean amplitude of the in-plane velocity component, $\langle \bar{v} \rangle$, with superposed in-plane velocity vectors at the LSC plane ($d_{\mathrm{LSC}}$) and the orthogonal one ($d_{\mathrm{O}}$), for $Ra = 2 \times 10^7$. (a) RBC. (b) FS. The downward motion of the water is stronger and the upper counter-rotating vortices are larger in FS than in RBC.

but instead extends throughout the domain.

Finally, it is worth mentioning that in the context of our study we have performed simulations at a higher Rayleigh number, namely, $Ra = 1 \times 10^8$. Our simulations predicted similar flow properties and the same differences between RBC and FS as the ones elaborated above.

### *4.2. Reorientation characteristics*

In this section we elaborate on the main features and the frequency of reorientation events. The simulations are run for a long time period, 15 000 $t_{\mathrm{ff}}$, so as to register a sufficiently large number of reorientations in each case. This allows us to derive reliable estimates of the frequency of these events and to determine the effect of the free surface on them.

As mentioned in section 1, reorientations events are classified as rotations or cessations. In rectangular cavities, there are two types of rotations. The

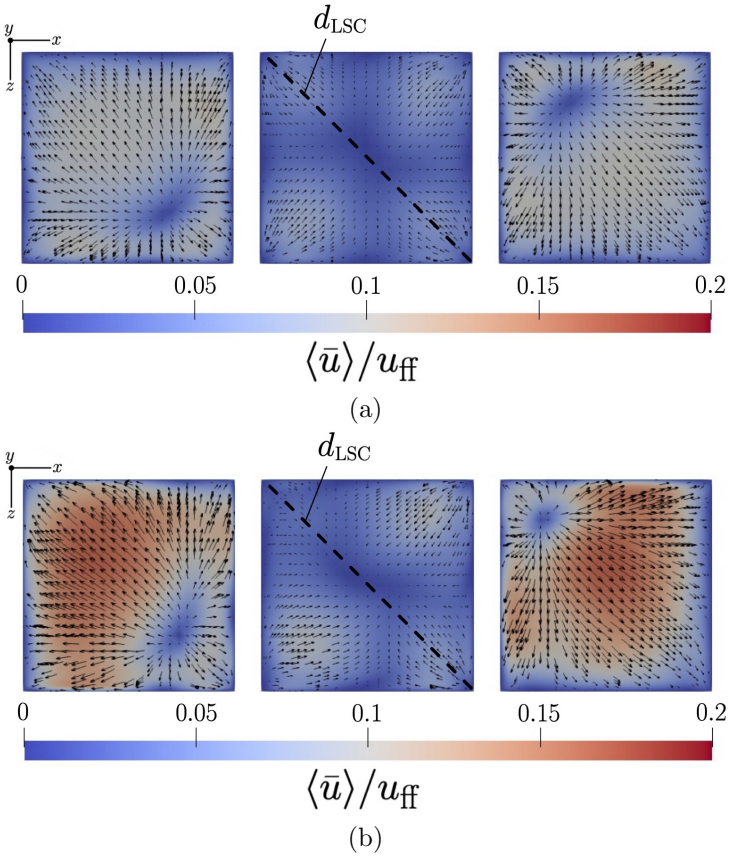
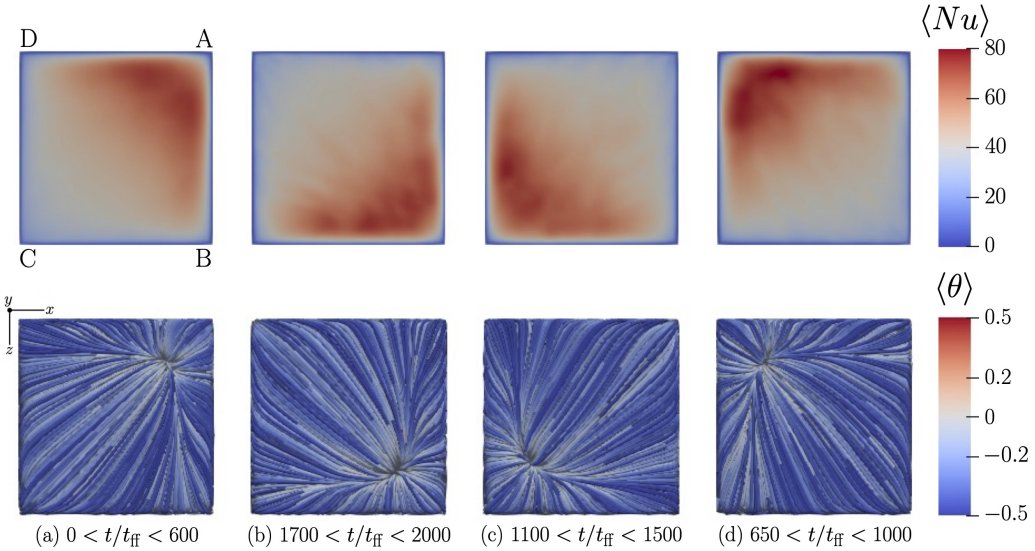



Figure 3: Colour plot of the mean amplitude of the horizontal velocity component $\langle \bar{u} \rangle$, superposed with the corresponding vector plots, at horizontal planes for $Ra = 2 \times 10^7$. The horizontal planes are $y/h = 0.95$ (left), $y/h = 0.5$ (middle) and $y/h = 0.05$ (right). (a) RBC. (b) FS. The presence of the free surface results in higher horizontal-velocity amplitudes at all horizontal planes.

first type consists of the change of alignment of the LSC from one diagonal plane to the other, whereas the second type consists of the inversion of the direction of the fluid motion within the LSC. Accordingly, the first type corresponds to a rotation of the LSC plane by an angle of $\pm\pi/2$ rads, whereas the second type corresponds to a rotation by an angle of $\pi$ rads. On the other hand, cessations involve the temporary shutoff of the LSC and its reappearance at another diagonal plane.

Time-averaged streamlines and local Nusselt number, $\langle Nu \rangle$, at the upper boundary are particularly useful for identifying the orientation of the LSC.

More specifically, the streamlines highlight the direction of the flow. Whereas the local $\langle Nu \rangle$ measures the strength of the convective motions and is higher in the neighborhood of the impingement point. As an example, in Figure 4, we provide plots of time-averaged streamlines and local $\langle Nu \rangle$ at the free surface over 4 different time periods for FS at $Ra = 1 \times 10^8$. During each of the 4 selected time periods the LSC was stable, *i.e.* no reorientation events took place. One can observe that during the simulation, the LSC has assumed all possible orientations. Our simulations predicted similar streamlines and local $\langle Nu \rangle$ distribution for all cases studied herein, namely, RBC and FS at $Ra = 2 \times 10^7$ and $Ra = 1 \times 10^8$.




(a) $0 < t/t_{\text{ff}} < 600$ (b) $1700 < t/t_{\text{ff}} < 2000$ (c) $1100 < t/t_{\text{ff}} < 1500$ (d) $650 < t/t_{\text{ff}} < 1000$

Figure 4: FS and $Ra = 1 \times 10^8$. Time-averaged streamlines and local $\langle Nu \rangle$ at the free surface for the four possible orientations of the flow. Each time period mentioned above is the duration of the corresponding LSC orientation.

In order to compute the time periods during which the LSC is stable, *i.e.* it remains at the same diagonal plane, we have employed probes to record the time series of the vertical velocity component $v$ at specific points. This technique has been previously used in experiments (with thermistors as probes) [14, 39] and in numerical simulations [2, 8, 16]. In our study, the probes have been distributed in the same manner as in [2]. More specifically, we have placed 8 probes at each of the following horizontal planes: $y/h = 0.25$, $y/h = 0.5$ and $y/h = 0.75$. The probes of each plane are located at

azimuth angles of $\frac{i\pi}{4}$, $i = 1...8$ and at a distance of $0.1h$ from their adjacent vertical wall, as shown in Figure 5. It should be noted that using 8 probes at each plane, instead of merely the 4 corner ones, provides more robust estimates of the reorientation events.

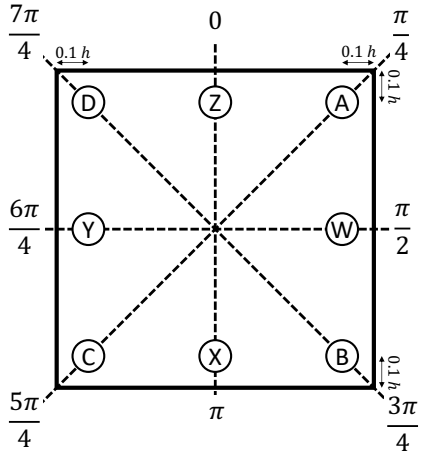



Figure 5: Horizontal plane showing the position of 8 probes. Probes are placed at three horizontal planes ($y/h = 0.25$, $y/h = 0.5$ and $y/h = 0.75$) for a total of 24 probes.

In Figures 6 and 7 we present the time series of the vertical velocity component $v$ at the corner probes (A, B, C and D) of the mid-height plane, $y/h = 0.5$. In particular, Figure 6 shows the time series of $v$ for RBC at $Ra = 1 \times 10^8$, whereas Figure 7 shows the equivalent time series for FS and at the same $Ra$. According to these plots, when the LSC is aligned with a particular diagonal plane, the probes located therein record vertical velocities of the same order of magnitude but of opposite sign; see also Figures 2a & 2b. On the other hand, the probes located at the orthogonal diagonal plane record vertical velocities of equal magnitude and zero mean. As pointed out in [2], this is characteristic of the counter-rotating vortices at the orthogonal plane.

In order to register reorientation events, one can compute the so-called amplitude $\delta$ and azimuth angle $\phi$ of the LSC. To this end, we employ herein the method of Cioni et al. [16] which is based on the azimuthal Fourier transform; this method has also been used in [2]. According to it, on the basis of the dimensionless vertical velocity and azimuth angle of each probe at

mid-height, $v_i$ and $\theta_i$ respectively, one can compute the following quantities,

$$A_1(t) \;=\; \frac{1}{2}\sum_{j=1}^{8} v_i(t)\cos(\theta_i)\,, \qquad B_1(t) \;=\; \frac{1}{2}\sum_{j=1}^{8} v_i(t)\sin(\theta_i)\,. \tag{17}$$

Then, $\delta$ and $\phi$ are respectively given by,

$$\delta(t) \;=\; \sqrt{A_1^2(t)+B_1^2(t)}\,, \qquad \phi(t) \;=\; sgn\left(B_1(t)\right)\;\cos^{-1}\left(\frac{A_1(t)}{|\delta(t)|}\right)\,. \tag{18}$$

Significant changes of $\phi(t)$ signal a reorientation event. On the other hand, $\delta$ provides information about the strength of fluid motion in the LSC and, therefore, allows to distinguish rotations from cessations. More specifically, when a cessation takes place, $\delta$ drops considerably before recovering its mean value. On the other hand, the value of $\delta$ does not change significantly during rotations.

The time series of $\delta$ and $\phi$ for RBC and FS at $Ra = 1\times10^8$ are shown in Figures 6 and 7, respectively. In these figures we can readily observe the change of $v$ in diagonal probes as well as changes in $\phi$; such changes mark reorientation events. It is worth mentioning that the numerous isolated spikes that appear in the time series of $\phi$ are due to individual plumes escaping from the LSC. Therefore, these isolated spikes are irrelevant to reorientation events [40].

In this manner, the time series of $\phi$, $\delta$ and $v$ at $y/h = 0.5$ allow to determine the orientation of the LSC and properly classify a reorientation event. For example, let us consider the case FS at $Ra = 1\times10^8$ for $0 < t < 580\,t_{\rm ff}$. In the upper half of Figure 7, one can see that the vertical velocity component $v$ is positive at probe A and negative at probe C, whereas it oscillates around zero at probes B and D. Also, from the time series of $\phi$ in the lower part of Figure 7 we confirm that the orientation of the LSC remains fixed during this time period. From these pieces of information we conclude that the azimuth angle of the LSC plane is $\pi/4$ rads.

The probes located at the lower and upper horizontal planes, $y/h = 0.25$ and $y/h = 0.75$ respectively, can be used to further analyze the evolution of the LSC with time. For FS at $Ra = 10^8$, the time series of the vertical velocity component $v$ recorded by the corner probes of these planes are plotted in Figure 8. The corner probes record peaks of the signal of $v$ whenever the impingement point of the LSC is located in their neighborhood. More specifically, the two probes located at the LSC diagonal record either positive peaks

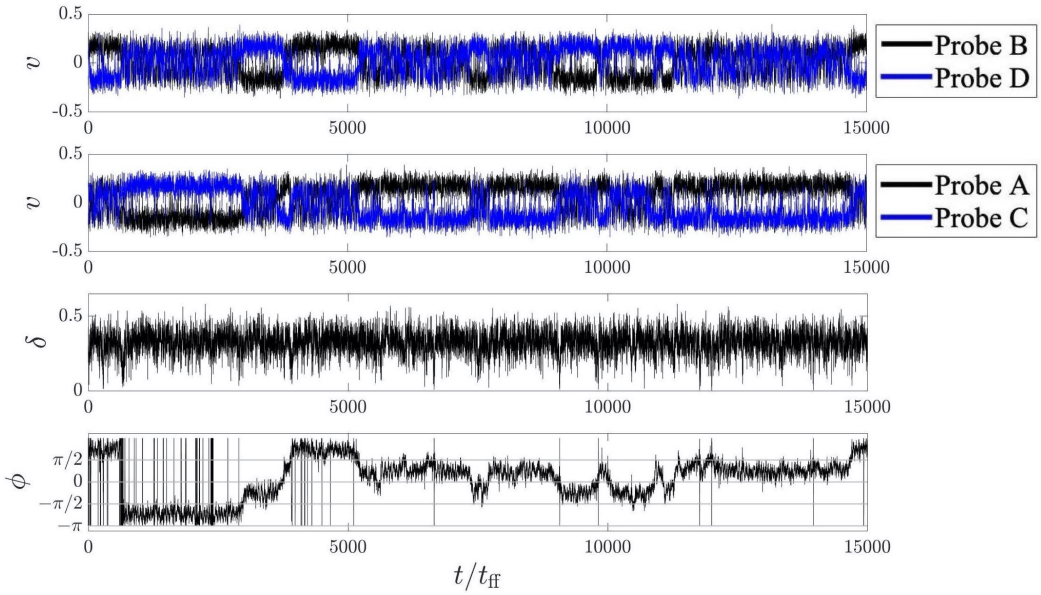



Figure 6: Standard RBC at $Ra = 1 \times 10^8$. Time series of the dimensionless vertical velocity $v$, amplitude $\delta$ and azimuth angle $\phi$ of the LSC, recorded by probes of the mid-height plane, $y/h = 0.5$.

in the upper plane or negative ones in the lower one. When a corner probe of the upper horizontal plane and the LSC diagonal plane records peaks of a given sign, then the juxtaposed probe at the lower horizontal plane records peaks of the opposite sign. On the other hand, the probes located at the orthogonal diagonal plane will not register any peaks at either the lower or the upper plane.

Considering the example given above, *i.e.* the A-C orientation of the LSC between $0 < t < 580\, t_{\rm ff}$ for the FS case at $Ra = 1 \times 10^8$, one can also use the time series of $v$ at $y/h = 0.25$ and $y/h = 0.75$ to identify the orientation of the LSC. Indeed, in Figure 8 and for $0 < t < 580\, t_{\rm ff}$, we can observe the recording of positive peaks at the upper probe A and lower peaks at the lower probe C. We can therefore conclude that, in the vicinity of probe A the fluid in the LSC moves upward, whereas in the vicinity of probe C it moves downward.

By applying the above methodology to the time series generated by our simulations, we have confirmed that reorientation events of the LSC occur quite often. However, these events occur in a spontaneous and apparently

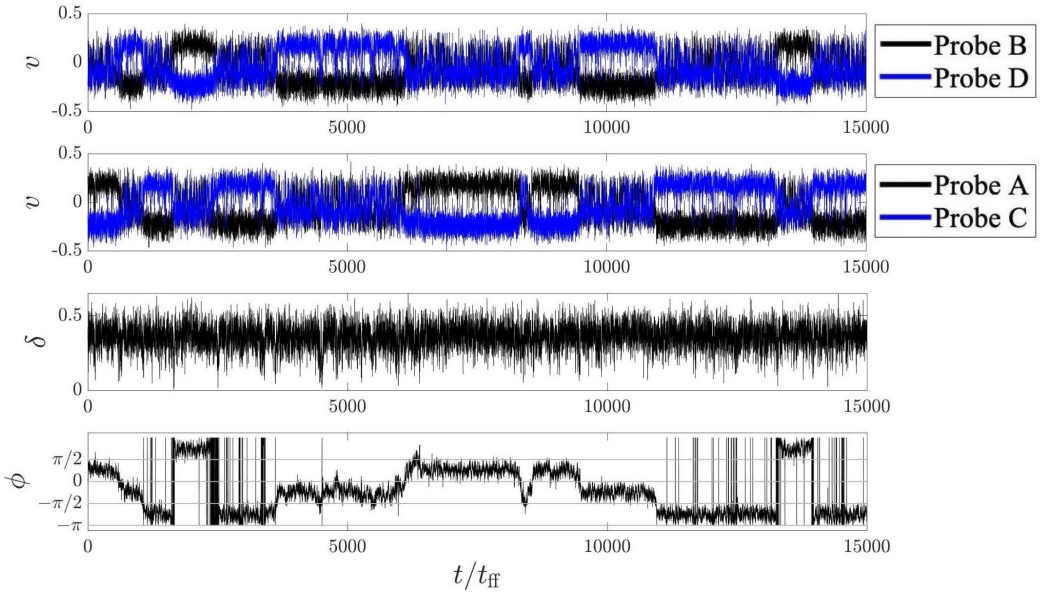



Figure 7: FS at $Ra = 1 \times 10^8$. Time series of the dimensionless vertical velocity $v$, amplitude $\delta$ and azimuth angle $\phi$ of the LSC, recorded by probes of the mid-height plane, $y/h = 0.5$.

random manner. Further, according to the plots in Figures 6 and 7, the amplitude $\delta$ oscillates significantly around its mean value, which implies that rotations of the LSC from one diagonal plane to the other are the most frequent ones. On the other hand, inversion of the direction of fluid motion within the LSC (rotation of $\pi$ rads) are particularly scarce. During the duration of the simulations, 15 000 $t_{\mathrm{ff}}$, such inversions occurred very rarely when $Ra = 2\times10^7$ and did not occur at all when $Ra = 1\times10^8$. It is also worth adding, that the rotation process is similar for both classical RBC and FS, *i.e.* corner roll increase, break of the main roll and finally, re-organization of the flow. For more details on the various stages of LSC rotations in classical RBC, the reader is referred to [11].

Further, the plots in Figures 6 and 7 show that $\delta$ occasionally drops to zero, which is the trademark sign of a cessation event. Such events can be readily identified in Figures 9a (RBC) and 9b (FS) which depict close-ups of the time series of $\delta$ and $\phi$. In these plots, we can clearly observe that at some time $\delta$ drops significantly. Subsequently it increases again and eventually reaches its previous levels. During the period that the value of $\delta$

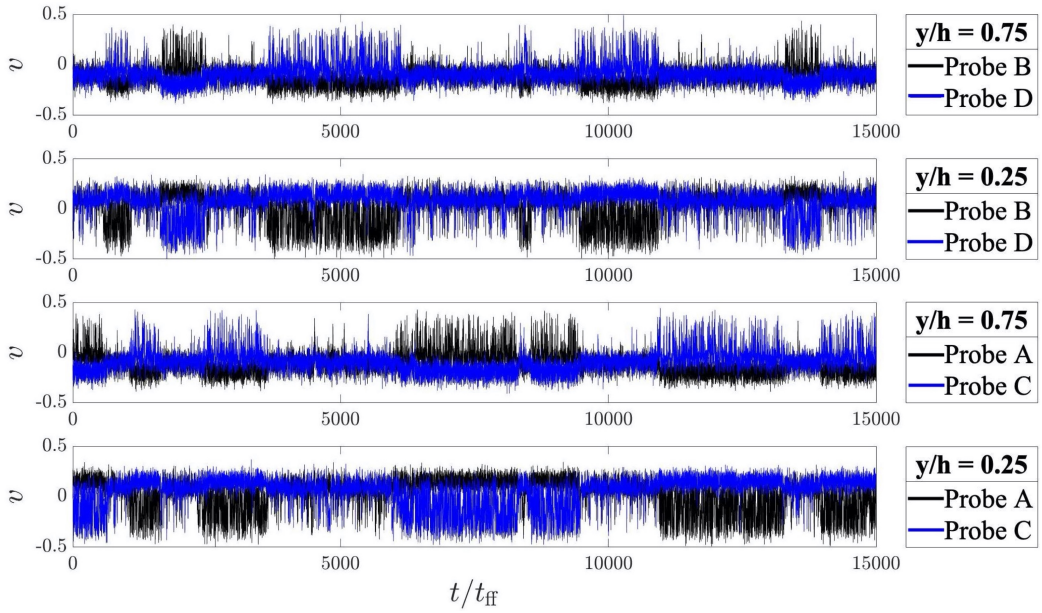



Figure 8: FS at $Ra = 1 \times 10^8$. Time series of the dimensionless vertical velocity $v$, recorded by the corner probes of the upper ($y/h = 0.75$) and lower ($y/h = 0.25$) planes.

is very small, the angle $\phi$ exhibits very large gradients, which implies absence of a clear orientation of the fluid circulation. Eventually though, $\phi$ stabilizes again. As mentioned above, this behavior of $\delta$ and $\phi$ implies that the LSC circulation temporarily shuts off before it emerges again. In other words, this is a cessation event. Nonetheless it should be added that cessation events are less frequent than rotations. According to our study, cessations account for approximately 15% of the reorientation events, all the others being rotations.

In Table 4 we provide the number of reorientation events over a time period of 15 000 $t_{\mathrm{ff}}$ for each of the 4 cases examined in our study, *i.e.* RBC and FS at $Ra = 2 \times 10^7$ and $Ra = 1 \times 10^8$. It is interesting to observe that, at both $Ra$, the number of reorientations in RBC and FS are very close. We therefore conclude that the presence of the free surface does not have any significant effect in the frequency of reorientations.

We further note that the number of reorientations drops significantly with $Ra$. In other words, higher turbulence intensities tend to suppress reorientation events. The same trend was predicted in [40] and [11], the authors of which examined convection of air in cylindrical and cuboidal domains, respectively. In particular, the authors of [11] observed that the corner rolls

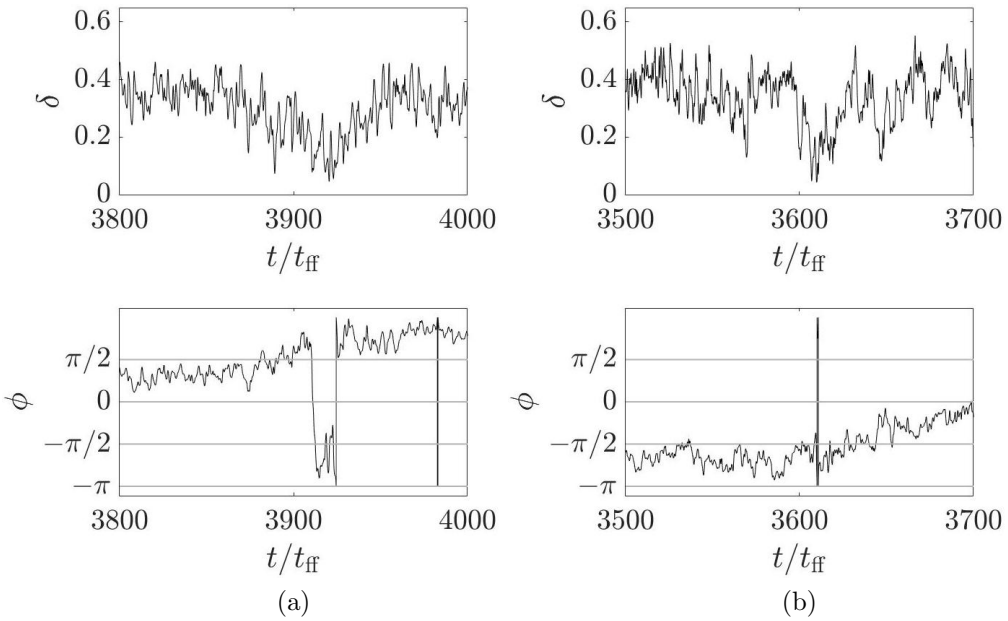



Figure 9: Close-ups of the time series of the amplitude $\delta$ and orientation $\phi$ of the LSC during a cessation event at $Ra = 1 \times 10^8$. (a) RBC. (b) FS. During a cessation, the amplitude $\delta$ drops significantly while the angle $\phi$ exhibits very large gradients.

shrink as $Ra$ increases. This, in turn, leads to a more dominant LSC in the diagonal plane, hence less frequent reorientation events.

| $Ra$ | Type | $N_{\mathrm{r}}$ | $f_{\mathrm{r}}$ |
|---|---|---|---|
| $2 \times 10^7$ | RBC | 37 | 0.0025 |
| | FS | 37 | 0.0025 |
| $1 \times 10^8$ | RBC | 14 | 0.0009 |
| | FS | 12 | 0.0008 |

Table 4: Total number of reorientation events, $N_{\mathrm{r}}$ over a time period of 15 000 $t_{\mathrm{ff}}$ and corresponding reorientation frequencies $f_{\mathrm{r}}$.

In Figure 10 we present plots of the cumulative number of reorientations with time. It is worth observing that even though these events occur spontaneously and in an apparently random fashion, their frequency, remains constant with time. Moreover, the reorientation frequency is very similar for RBC and FS and depends only on $Ra$. Accordingly, the cumulative number of reorientations can be very well approximated by a single linear fit for each

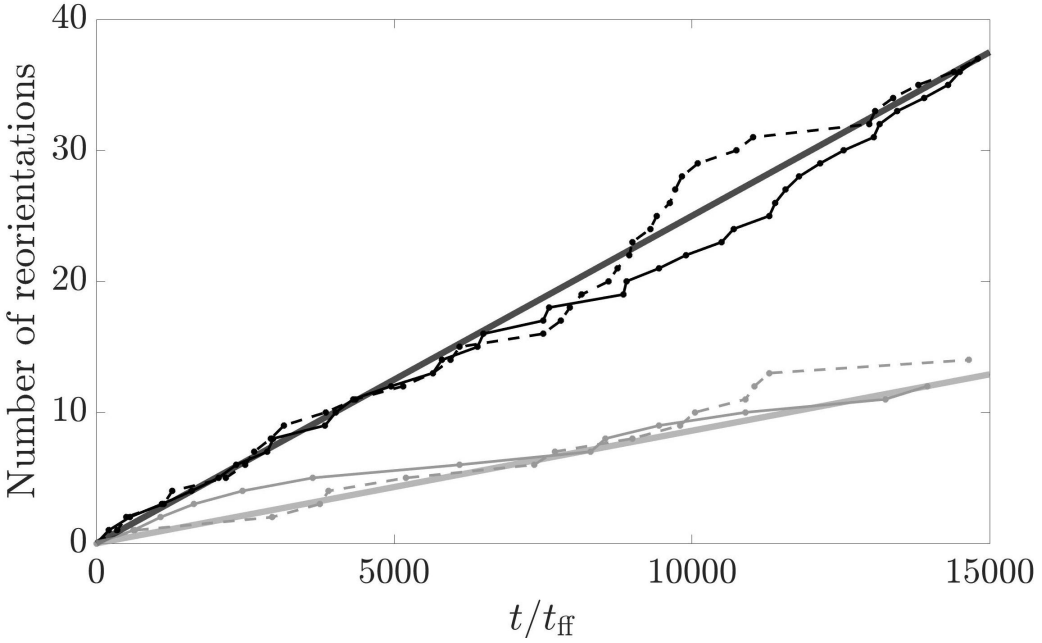



Figure 10: Cumulative number of reorientation events with time. Black lines are for $Ra = 2 \times 10^7$: FS (——) and RBC (– –). Grey lines are for $Ra = 1 \times 10^8$: FS (——) and RBC (– –). The dots signal the occurrence of a reorientation. Also, the thick solid lines are linear fits of the cumulative numbers of reorientations for FS at $Ra = 2 \times 10^7$ (▬) and $Ra = 1 \times 10^8$ (▬).

$Ra$, *i.e.* independently of the upper boundary condition, as shown in Figure 10.

The reorientation frequencies, $f_{\mathrm{r}}$, for the cases examined herein are also listed in Table 4. It should be noted that $f_{\mathrm{r}}$ is derived by using the free-fall time $t_{\mathrm{ff}}$ as the reference time unit. The rationale for this choice is that $t_{\mathrm{ff}}$ does not depend on the upper boundary condition and therefore allows for comparisons between RBC and FS.

On the other hand, in the study of reorientations in RBC of air [2], the reference time unit was the eddy turnover time, $t_{\mathrm{eddy}}$. Therein, $t_{\mathrm{eddy}} = 7$ s and the reorientation frequency at $Ra = 1 \times 10^8$ was predicted to be 0.016 events per $t_{\mathrm{eddy}}$ or, equivalently, 0.0029 events per s. However for RBC at $Ra = 1 \times 10^8$, and for $t_{\mathrm{ff}} = 0.856$ s, our simulations predicted a frequency of 0.0011 events per s. It should be noted that the working medium in [2] was air at $Pr = 0.7$, whereas in our study it is water at $Pr = 2.23$. This suggests that the reorientation frequency reduces with the Prandtl number.

It is noted that, according to the numerical study [10], the reorientation frequency does not exhibit monotonic behavior with the Prandtl number. However, the study [10] involved 2D simulations in circular geometries and, therefore, its results may not be applicable to the problem examined herein, which is turbulent convection in rectangular domains. In summary, more simulations at different $Pr$ are needed in order to conclusively establish the trend of the reorientation frequency over a broad range of Prandtl numbers.

*4.3. Turbulence statistics*

In this subsection we turn our attention to the influence of reorientation events on turbulence statistics. To this end, statistics are taken over different time periods, referred to herein as "averaging times", ranging from 500 $t_{\mathrm{ff}}$ to 15 000 $t_{\mathrm{ff}}$. All quantities presented in this subsection are time- and area-averaged. Our analysis focuses on second-order statistics.

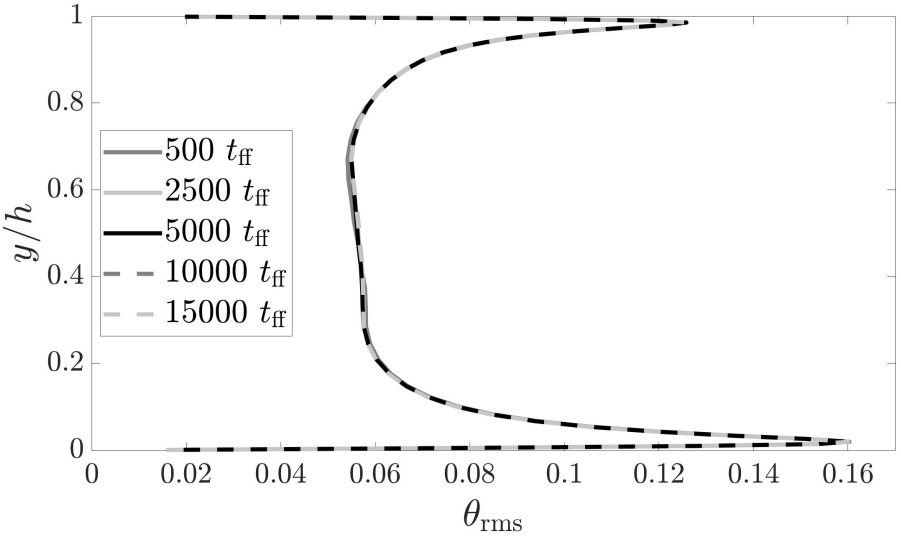



Figure 11: Profiles of $\theta_{\mathrm{rms}}$ for FS at $Ra = 2 \times 10^7$, averaged over different time periods.

The first profile understudy is the root-mean-square (rms) of the normalized temperature, $\theta_{\mathrm{rms}}$, which is defined as $\theta_{\mathrm{rms}} = \sqrt{\langle\theta^2\rangle_{xz} - \langle\theta\rangle_{xz}^2}$. As stated above, $\langle\,\rangle_{xz}$ denotes a time- and area-averaged quantity. In Figure 11, we present plots of $\theta_{\mathrm{rms}}$ for FS at $Ra = 2 \times 10^7$ over different averaging times. We first remark that the profiles in FS are not symmetric with respect to the mid-height location, contrary to RBC [41, 42, 43, 44, 41]. More specifically,

in FS the values in the lower half of the domain are higher than in the upper half. This is also true for the peaks of $\theta_{\text{rms}}$ near the boundaries. Also, on the basis of the locations of these peaks, we infer that in FS the upper thermal boundary layer is considerably thinner than the lower one.

On the other hand, our analysis showed that in FS, similarly to RBC, the values of $\theta_{\text{rms}}$ in the bulk are decreased and the thermal boundary layers become thinner as $Ra$ is increased.

With regard to the impact of reorientation events, we remark that the profiles of $\theta_{\text{rms}}$ do not evolve as the averaging time increases. Temperature second-order statistics are therefore not affected by reorientations.

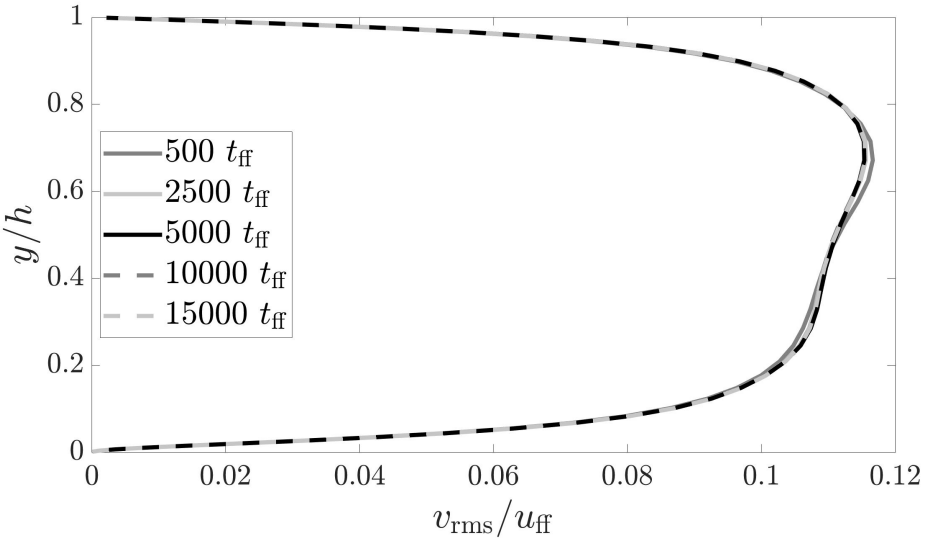



Figure 12: Profiles of $v_{\text{rms}}$ for FS at $Ra = 2 \times 10^7$, averaged over different time periods.

Similar remarks hold for the rms of the vertical velocity component. Figure 12 depicts plots of the rms of the vertical velocity component, $v_{\text{rms}} = \sqrt{\langle v^2 \rangle_{xz} - \langle v \rangle_{xz}^2}$. The profiles in FS are asymmetric and present higher values in the upper half of the domain whereas RBC would have presented a parabolic shape. Furthermore, the profiles do not evolve with increasing averaging time, showing that $v_{\text{rms}}$ is independent of reorientation events.

Finally, in Figure 13 we present plots of the rms of the horizontal velocity components, $\bar{u}_{\text{rms}} = \sqrt{\langle u^2 \rangle_{xz} - \langle u \rangle_{xz}^2 + \langle w^2 \rangle_{xz} - \langle w \rangle_{xz}^2}$. As reorientations are characterized by a change of direction of the flow, the horizontal velocities are greatly affected by these events. We readily observe that the values in

the bulk of $\bar{u}_{\mathrm{rms}}$ increase and become more uniform as the averaging time increases. In fact, the profile becomes practically flat in the bulk as more reorientations are taken into account. Also, the peaks at the free surface and at the bottom boundary layer increase with the averaging time. All these observations point out the fact that long averaging times are required for the rms of the horizontal velocity components to converge.

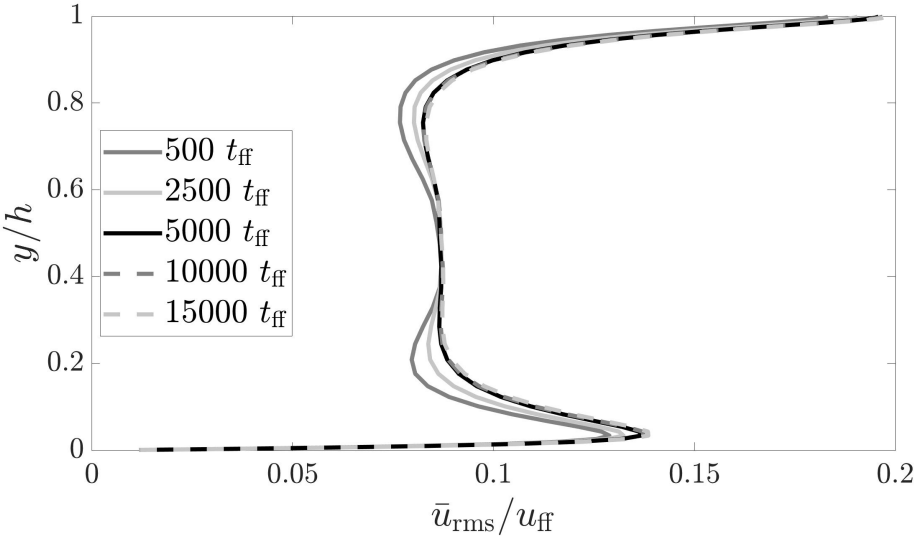



Figure 13: Profiles of $\bar{u}_{\mathrm{rms}}$ for FS at $Ra = 2 \times 10^7$, averaged over different time periods.

The analysis of turbulent statistics for the other three cases considered herein corroborated these observations. Evidently, when interpreting these results, one must take into account that statistics from LES are less accurate than those from direct numerical simulations. Nonetheless, the differences between the $\bar{u}_{\mathrm{rms}}$ profiles over different averaging times are quite significant. We may therefore conclude that reorientation events have a considerable impact on $\bar{u}_{\mathrm{rms}}$.

## 5. Conclusions

In this paper, we presented Large Eddy Simulations of turbulent thermal convection of water in a cube with a free-slip upper boundary. The objective of this work was to study the dynamics of the large-scale circulation (LSC), which is the principal convective structure in the flow of interest. For

comparison purposes, LES of the equivalent classical Rayleigh-Bénard Convection cases have also been performed. Our simulations confirmed that the free surface introduces a flow asymmetry that promotes convective motion in the bulk of the domain. Moreover, it results in higher velocities, not only in the LSC but also in the secondary vortical structures. Additionally, since the free surface promotes convection, it results in higher Nusselt numbers and a shift of the mean temperature profile towards the cold upper boundary.

A particularly intriguing feature of the LSC is its ability to switch its orientation plane. In order to explore the effects of the free surface on this phenomenon, we performed simulations over a long time period, 15 000 free-fall times, so as to record as many reorientation events as possible. Our simulations predicted that reorientation events occur spontaneously but their frequency remains constant with time. However, the reorientation frequency decreases substantially with the Rayleigh number. Also, the reorientation frequency in water is considerably lower compared to that in air. In other words, the frequency of reorientations events depends on the Prandtl number. On the other hand, the presence of the free surface has no significant effect on the reorientation frequency. Finally, our analysis showed that reorientation events have a significant impact on the second-order statistics of the horizontal velocity but not on those of the temperature and vertical velocity. In particular, the $\bar{u}_{\mathrm{rms}}$ values in the bulk tend to increase as more reorientation events are taken into account. Consequently, numerical convergence of the $\bar{u}_{\mathrm{rms}}$ profiles can be achieved only after long averaging times that account for a large number of reorientations.

**Acknowledgements**

The authors would like to thank Dr. William Hay for many fruitful discussions and suggestions. Further, they gratefully acknowledge the financial support provided by the Belgian Federal Ministry of Energy under the Energy Transition Fund, project SFP-LOCA. This work benefited from the computational resources provided by the supercomputing facilities of the Université catholique de Louvain (CISM/UCL) and the Consortium for high-performance computing and data storage of the Federation Wallonie Bruxelles (FWB), funded by the Belgian Fund of Scientific Research (F.R.S.-FNRS) under Convention No. 2.5020.11.

## References


[1] T. L. Bergman, A. S. Lavine, F. P. Incropera, D. P. DeWitt, Fundamentals of Heat and Mass Transfer, 7th ed., John Wiley & Sons, 2011.

[2] N. Foroozani, J. Niemela, V. Armenio, K. Sreenivasan, Reorientations of the large-scale flow in turbulent convection in a cube, Phys. Rev. E 95 (2017) 033107.

[3] R. Krishnamurti, L. Howard, Large-scale flow generation in turbulent convection, Proceedings of the National Academy of Sciences of the United States of America 78 (1981) 19811985.

[4] N. Foroozani, J. Niemela, V. Armenio, K. Sreenivasan, Influence of container shape on scaling of turbulent fluctuations in convection, Phys. Rev. E 90 (2014) 063003.

[5] N. Foroozani, J. Niemela, V. Armenio, K. Sreenivasan, Large eddy simulation of turbulent Rayleigh–Bnard convection in a cubic cell, in: ERCOFTAC Ser., Vol. 24, 2018, pp. 559–565.

[6] D. Giannakis, A. Kolchinskaya, D. Krasnov, J. Schumacher, Koopman analysis of the long-term evolution in a turbulent convection cell, J. Fluid Mech. 847 (2018) 735–767.

[7] W. A. Hay, M. V. Papalexandris, Numerical simulations of turbulent thermal convection with a free-slip upper boundary, Proc. R. Soc. A 475 (2019) 20190601.

[8] K. Sugiyama, R. Ni, R. J. A. M. Stevens, T. S. Chan, S.-Q. Zhou, H.-D. Xi, C. Sun, S. Grossmann, K.-Q. Xia, D. Lohse, Flow reversals in thermally driven turbulence, Phys. Rev. Lett. 105 (2010) 034503.

[9] A. Castillo-Castellanos, A. Sergent, B. Podvin, M. Rossi, Cessation and reversals of large-scale structures in square Rayleigh–Bnard cells, J. Fluid Mech. 877 (2019) 922–954.

[10] A. Xu, X. Chen, H.-D. Xi, Tristable flow states and reversal of the large-scale circulation in two-dimensional circular convection cells, Journal of Fluid Mechanics 910 (2021) A33. doi:10.1017/jfm.2020.964.

[11] V. T. Vishnu, A. K. De, P. K. Mishra, Dynamics of large-scale circulation and energy transfer mechanism in turbulent Rayleigh–Bnard convection in a cubic cell, Phys. Fluids 32 (2020) 095115.

[12] S. Cioni, S. Ciliberto, J. Sommeria, Experimental study of high-Rayleigh-number convection in mercury and water, Dynam. Atmos. Oceans 24 (1996) 117–127.

[13] P. Mishra, A. De, M. Verma, V. Eswaran, Dynamics of reorientations and reversals of large-scale flow in Rayleigh–Bnard convection, J. Fluid Mech. 668 (2011) 480–499.

[14] E. Brown, G. Ahlers, Rotations and cessations of the large-scale circulation in turbulent Rayleigh–Bénard convection, J. Fluid Mech. 568 (2006) 351–386.

[15] U. Hansen, D. A. Yuen, S. E. Kroening, Mass and heat transport in strongly time-dependent thermal convection at infinite prandtl number, Geophysical & Astrophysical Fluid Dynamics 63 (1992) 67–89.

[16] S. Cioni, S. Ciliberto, J. Sommeria, Strongly turbulent Rayleigh–Bnard convection in mercury: comparison with results at moderate prandtl number, J. Fluid Mech. 335 (1997) 111–140.

[17] J. Niemela, L. Skrbek, K. Sreenivasan, R. Donnelly, Turbulent convection at very high Rayleigh numbers, Nature 404 (2000) 837–40.

[18] K. Sreenivasan, A. Bershadskii, J. Niemela, Mean wind and its reversal in thermal convection, Physical review. E, Statistical, nonlinear, and soft matter physics 65 (2002) 056306.

[19] S. Paolucci, Filtering of sound from the Navier–Stokes equations, NASA STI/Recon Technical Report N 83 (1982) 26036.

[20] B. Lessani, M. V. Papalexandris, Time accurate calculation of variable density flows with strong temperature gradients and combustion, J. Comput. Phys. 212 (2006) 218–246.

[21] M. Georgiou, M. V. Papalexandris, Direct numerical simulation of turbulent heat transfer in a T-junction, J. Fluid Mech. 845 (2018) 581–614.

[22] M. V. Papalexandris, On the applicability of Stokes' hypothesis to low-Mach-number flows, Continuum Mech. Therm. 32 (2020) 1245–1249.

[23] E. W. Lemmon, M. L. Huber, M. O. McLinden, NIST Standard Reference Database 23: Reference Fluid Thermodynamic and Transport Properties - REFPROP, 9.0 ed., 2010.

[24] J. H. Ferziger, M. Perić, Computational Methods for Fluid Dynamics, 2nd ed., Springer, Berlin, 1999.

[25] W. Rodi, G. Constantinescu, T. Stoesser, Large-Eddy Simulation in Hydraulics, CRC Press, 2013.

[26] S. Pope, P. Eccles, S. Pope, C. U. Press, Turbulent Flows, Cambridge University Press, 2000. URL: https://books.google.be/books?id=HZsTw9SMx-0C.

[27] A. Yoshizawa, Statistical theory for compressible turbulent shear flows, with the application to subgrid modeling, Phys. Fluids 29 (1986) 2152–2164.

[28] W. W. Kim, S. Menon, A new dynamic one-equation subgrid-scale model for large eddy simulations, in: 33rd Aerospace Sciences Meeting and Exhibit, AIAA 95-0356, 1995.

[29] T. M. Eidson, Numerical simulation of the turbulent Rayleigh–Bénard problem using subgrid modelling, J. Fluid Mech. 158 (1985) 245–268.

[30] B. Lessani, M. V. Papalexandris, Numerical study of turbulent channel flow with strong temperature gradients, Int. J. Numer. Method. H 18 (2008) 545–556.

[31] C. M. Rhie, W. L. Chow, Numerical study of the turbulent flow past an airfoil with trailing edge separation, AIAA 21 (1983) 1525–1532.

[32] R. I. Issa, Solution of the implicitly discretized fluid flow equations by operator-splitting, J. Comp. Phys. 62 (1985) 40–65.

[33] P. J. Oliviera, R. I. Issa, An improved PISO algorithm for the computation of buoyancy driven flows, Numer. Heat Tr. B-Fund 40 (2001) 473–493.

[34] W. A. Hay, M. V. Papalexandris, Evaporation-driven turbulent convection in water pools, J. Fluid Mech. 904 (2020) A14.

[35] O. Shishkina, R. Stevens, S. Grossmann, D. Lohse, Boundary layer structure in turbulent thermal convection and its consequences for the required numerical resolution, New J. Phys. 12 (2010) 075022.

[36] W. A. Hay, J. Martin, B. Migot, M. V. Papalexandris, Turbulent thermal convection driven by free-surface evaporation in cuboidal domains of different aspect ratios, Phys. Fluids 33 (2021) 015104.

[37] R. Stevens, R. Verzicco, D. Lohse, Radial boundary layer structure and Nusselt number in Rayleigh–Bnard convection, J. Fluid Mech. 643 (2010) 495–507.

[38] M. Kaczorowski, K.-Q. Xia, Turbulent flow in the bulk of Rayleigh–Bnard convection: small-scale properties in a cubic cell, J. Fluid Mech. 722 (2013) 596–617.

[39] E. Brown, A. Nikolaenko, G. Ahlers, Reorientation of the large-scale circulation in turbulent Rayleigh–Bnard convection, Phys. Rev. Lett. 95 (2005) 084503.

[40] S. Wagner, O. Shishkina, C. Wagner, Boundary layers and wind in cylindrical Rayleigh–Bnard cells, J. Fluid Mech. 697 (2012) 336–366.

[41] Q. Zhou, K.-Q. Xia, Thermal boundary layer structure in turbulent Rayleigh–Bnard convection in a rectangular cell, J. Fluid Mech. 721 (2013) 199–224.

[42] J. Wang, K.-Q. Xia, Spatial variations of the mean and statistical quantities in the thermal boundary layers of turbulent convection, Phys. Condens. Matter 32 (2003) 127–136.

[43] R. Kunnen, B. Geurts, H. Clercx, Direct numerical simulation of turbulent rotating Rayleigh–Bnard convection, in: Direct and Large-Eddy Simulation VI. Springer, 2006, pp. 233–240.

[44] S.-H. Peng, K. Hanjalic, L. Davidson, Large-eddy simulation and deduced scaling analysis of Rayleigh-Bnard convection up to ra = 109, J. Turbul. 7 (2006).